Spatial enrichment of the type 1 interferon signature in the brain of a neuropsychiatric lupus murine model

Ernest Aw [a,b,1,**], Stacie L. Lin [a,b,**], Yingying Zhang[a], Uli Herrmann[a], Esra Yalcin[a], Kent Langston[c] , Carlos Castrillion[a,2], Minghe Ma[a], Jeffrey R. Moffitt[a,d], Michael C. Carroll [a,*]

[a] Program in Cellular and Molecular Medicine, Boston Children's Hospital, Harvard Medical School, Boston, MA, United States

[b] Division of Medical Sciences, Harvard Medical School, Boston, MA, United States

[c] Department of Immunology, Harvard Medical School and Evergrande Center for Immunologic Diseases, Harvard Medical School and Brigham and Women's Hospital, Boston, MA, USA

[d] Department of Microbiology, Harvard Medical School, Boston, MA, USA

[1] Present address: Thelper AS, Oslo Cancer Cluster Incubator AS, Ullernchausséen 64, 0379 Oslo, Norway

[2] Present address: Department of Medicine, Division of Rheumatology, Emory University, Atlanta, GA, USA

[*] Corresponding author: e-mail address: michael.carroll@childrens.harvard.edu

[**] Co-first authors

Declarations of interest: none

Highlights

- Mouse model exhibits neuropsychiatric behaviors and elevated type 1 interferon.

- The type 1 interferon gene signature is predominantly upregulated in the brain.

- Interferon-stimulated genes (ISGs) are present in a spatial pattern in the brain.

- Cellular and synaptic interactions are generally repressed in cells with high ISGs.

Keywords

Interferon alpha (IFNα), interferon-stimulated gene (ISG), neuropsychiatric, glial cells,

spatial transcriptomics, single-nucleus sequencing

Abstract

Among systemic lupus erythematosus (SLE) patients, neuropsychiatric symptoms are highly prevalent, being observed in up to 80% of adult and 95% of pediatric patients. Type 1 interferons, particularly interferon alpha (IFNα), have been implicated in the pathogenesis of SLE and its associated neuropsychiatric symptoms (NPSLE). However, it remains unclear how type 1 interferon signaling in the central nervous system (CNS) might result in neuropsychiatric sequelae. In this study, we validate an NPSLE mouse model and find an elevated peripheral type 1 interferon signature alongside clinically relevant NPSLE symptoms such as anxiety and fatigue. Unbiased single-nucleus sequencing of the hindbrain and hippocampus revealed that interferon-stimulated genes (ISGs) were among the most highly upregulated genes in both regions and that gene pathways involved in cellular interaction and neuronal development were generally repressed among astrocytes, oligodendrocytes, and neurons. Using image-based spatial transcriptomics, we found that the type 1 interferon signature is enriched as spatially distinct patches within the brain parenchyma of these mice. Our results suggest that type 1 interferon in the CNS may play an important mechanistic role in mediating NPSLE behavioral phenotypes by repressing general cellular communication pathways, and that type 1 interferon signaling modulators are a potential therapeutic option for NPSLE.

1. Introduction

Systemic lupus erythematosus (SLE) is a clinically heterogeneous and incurable autoimmune disease that affects multiple organs. The prevailing paradigm is that defective apoptotic cell clearance results in cellular debris leading not only to the production of autoantibodies but also triggering the receptors TLR7 and TLR9, thus leading to pathological type 1 interferon secretion by plasmacytoid and follicular dendritic cells (Lisnevskaia et al., 2014; Moulton et al., 2017; Crow, 2014; Das et al., 2017). In fact, chronic expression of a type 1 interferon signature in peripheral blood is found in up to 80% and 100% of adult and pediatric SLE patients, respectively, suggesting a key pathogenic role for type 1 interferons, particularly interferon alpha (IFNα) (Crow, 2014; Hua et al., 2006; Rodero et al., 2017).

While the kidney and skin are typical organ sites for SLE pathology, the central nervous system (CNS) is increasingly appreciated to be widely impacted, with clinical symptoms observed in up to 80% and 95% of adult and pediatric patients, respectively. These symptoms range from mild cognitive dysfunction and anxiety to overt psychosis and are collectively termed neuropsychiatric lupus (NPSLE) (Jeltsch-David and Muller, 2014; Kivity et al., 2015). While the pathophysiology of NPSLE is not well understood, inflammatory cytokines, neurotoxic autoantibodies, and vascular pathologies have all been proposed to contribute to NPSLE etiology (Aw et al., 2021; Jeltsch-David and Muller, 2014; Schwartz et al., 2019). Given its clinical heterogeneity, the cause of NPSLE is unlikely to be singly attributable to any one of these factors. However, we hypothesize that IFNα plays a significant role, given (1) the high prevalence of the type

1 interferon signature in patients, a signature that can be triggered by IFNα signaling through IFNAR and the JAK/STAT pathway (Schreiber and Piehler, 2015), (2) the increased levels of serum IFNα in lupus patients (Rodero et al., 2017), (3) the correlation between NPSLE and an elevated IFNα-associated gene signature in patient serum and cerebrospinal fluid (CSF) (Oke et al., 2019; Shiozawa et al., 1992), and (4) the similarity of neuropsychiatric sequelae experienced by patients treated with recombinant IFNα (Schaefer et al., 2002; Valentine and Meyers, 2005). Given the heterogeneity of clinical symptoms experienced by both NPSLE and other patients receiving therapeutic IFNα, we hypothesized that different brain regions and cell types were affected by IFNα, resulting in spatial enrichments of type 1 interferon signaling within the brain parenchyma that functionally determine behavioral outcomes.

Given the scarcity of NPSLE patient brain and peripheral tissue, animal models are critical for further study of the disease. There are few well-established murine models of NPSLE, and to the best of our knowledge, those that exist do not have existent or well-characterized peripheral type 1 interferon signatures (El Khoury et al., 2020; Zhuang et al., 2015a). The disease-accelerated *Sle1,Yaa* mouse exhibits key SLE pathological characteristics, such as high antinuclear autoantibody titers and severe glomerulonephritis, and has a 50% survival rate at 30 weeks of age (Subramanian et al., 2006). Derived by crossing the B6.*Sle1* strain with the BXSB strain, *Sle1,Yaa* mice have one copy of a segment of chromosome 1 that contains 3 subloci that promote various aspects of the autoimmune phenotype (originally derived from the lupus-susceptible NZM2410 strain) (Morel et al., 2001) and a translocation of a segment of the X chromosome onto the Y chromosome, resulting in the modified *Yaa* chromosome (Y-

linked autoimmune acceleration), which causes accelerated autoimmunity. Importantly, in *Sle1,Yaa* mice, the overexpression of *Tlr7* is thought to drive most of the accelerated autoimmune phenotypes (Fairhurst et al., 2008). Given the role of TLR7 signaling in generating the type 1 interferon response (Uematsu and Akira, 2007), we hypothesized that the *Sle1,Yaa* strain would likely exhibit the same elevated peripheral blood interferon signature seen in patients, as well as disease-associated sickness behaviors (neuropsychiatric symptoms). In this study, we validated the presence of a peripheral type 1 interferon signature and show clinically relevant anxiety- and fatigue-like behaviors in *Sle1,Yaa* mice. Strikingly, we also found that the type 1 interferon signature is elevated in the CNS of these mice and that it is spatially segregated in patches that are enriched within the subcortical areas. Thus, these results lay the foundation for further investigation of CNS IFNAR signaling in NPSLE.

2. Materials and Methods

2.1. Animals

Sle1,Yaa (021569), C57BL/6J (000664), and CD45.1 (002014) mice were purchased from Jackson Laboratories and bred in-house. *Ifnar1*^{-/-} (032045-JAX) mice were purchased from Jackson Laboratories/MMRRC and bred in-house. Male mice were exclusively used for all experiments due to the *Yaa* mutation on the Y-chromosome. *Sle1*^{-/-} and *Sle1*^{+/+}*,Yaa* mice were generated in-house as depicted in Supplementary Figure 4A. Mice were maintained at Harvard Medical School in an American Association for the Accreditation of Laboratory Animal Care–accredited facility. All animal experiments were approved by the Boston Children's Hospital and Harvard Medical

School institutional animal use and care committee in accordance with NIH guidelines for the humane treatment of animals.

2.2. Autoantibody quantification

Serum autoantibodies were quantified using the Luminex xMAP platform (Luminex) with the MILLIPLEX MAP Human Autoimmune Autoantibody Panel (HAIAB-10K, Millipore Sigma) following the manufacturer's instructions.

2.3. Behavioral phenotyping

All behavioral analyses except the treadmill fatigue test were performed in the Harvard Medical School Mouse Behavior Core facility. Mice were acclimated for at least 30 minutes prior to behavioral testing in a holding room, and all testing was carried out between the hours of 0800 – 1200 EST. The tests for Figure 2 and Supplementary Figures 2-4 were carried out in the following order over 7 days: Bright open field, Elevated plus maze, Light-dark box, Locomotor, Rotarod, Grip strength/Wire hang, Gait. The treadmill fatigue test was performed in a separate cohort of mice for these figures.

2.3.1. Bright Open Field

The bright open field test was used to measure anxiety-like behavior in mice (Yilmaz et al., 2021).

2.3.2. Elevated Plus Maze

The elevated plus maze (EPM) was used to measure anxiety-like behavior in mice. The EPM setup consisted of two open and two closed arms (30x5cm each) extended out from a central platform. The maze surface is elevated 46cm above the ground. All tests were carried out in dim ambient lighting. Mice were placed in the center platform of the

maze, facing an open arm, and allowed to explore the apparatus for 5 minutes. A computer-assisted video-tracking system (EthoVision XT, Noldus) was used to record the number of open and closed arm entries as well as the distance traveled and total time spent in either arm of the maze.

2.3.3. Light-Dark Box

The light-dark box test was used to measure anxiety-like behavior in mice. The experimental setup was an open field chamber measuring 27x27cm (Med Associates) that was equally portioned into two chambers with an opening in between (Yilmaz et al., 2021).

2.3.4. Locomotor Activity

Various parameters (ambulatory distance and vertical counts) of mouse activity in an open field chamber (Med Associates) were used to measure general locomotive behavior. Mice were placed in a chamber of dimensions 27x27x20cm and allowed to explore *ad libitum* for 1 hour. A computer-assisted infrared tracking system and software (Activity Monitor, Med Associates) was used to record the number of beam breaks as proxy measures for ambulatory distance and vertical counts. Room lights were dimmed to 20 lux to create a low-stress environment.

2.3.5. Rotarod

The rotarod apparatus (Ugo Basile) was used to assay fatigue-like and/or sensorimotor coordination phenotypes in mice (Yilmaz et al., 2021).

2.3.6. Grip Strength

Aggregate limb and forelimb grip strength was measured using a force transducer (Bioseb). Four independent measurements are performed, and the average was taken. Weight normalized strength was calculated by the following: *force transduced (g) / body weight (g)* (Schroeder et al., 2021).

2.3.7. Wire Hanging

The wire hanging test was used to measure muscular endurance in mice. Mice were placed onto the center of a wire grill measuring 75x75cm, with the wire <1mm in diameter. The grill was inverted at 90cm above ground, and the latency to fall was measured. Cotton pads were placed on the ground to minimize blunt trauma after falling. The maximum time on the wire grill was capped at 10 minutes. The holding impulse was calculated by the following: *latency to fall (s) * body weight (kg) * standard gravity (m/s^2)*.

2.3.8. Gait

The gait test was used to measure sensorimotor coordination in mice. Briefly, mice were placed on a treadmill at a constant speed of 13cm/s, and movement patterns were captured and analyzed by a high frame rate camera and commercial software (TreadScan, CleverSys Inc.). Coordination across multiple axes (longitudinal, lateral, and body rotation) was measured by the standard deviation from the mean per mouse.

2.3.9. Treadmill Fatigue

The treadmill fatigue test was adapted and modified (Dougherty et al., 2016) as a measure of fatigue-like behavior. Mice were acclimatized to the treadmill (Columbus Instruments Exer 3/6 Treadmill) for 2 consecutive days prior to testing. Paper towels were threaded through holes in the treadmill lid, spaced approximately one mouse

body-length from the shock grid, in order to provide an innocuous cue as a surrogate for electrical shock. The distance between the paper towel inserts and the shock grid was defined as the fatigue zone. On day 1, mice were allowed to explore for 5 minutes on the treadmill without the shock grid on. After 5 minutes, the shock grid was powered on (1.5 mA, 3 Hz), and the treadmill belt speed was set to 6m/min. After 5 minutes, the belt speed increased 2m/min every 2 min in a stepwise pattern, to a maximum of 10m/min for 5 minutes, before stopping the treadmill. Mice again explored the treadmill for 2 minutes without shock. Day 2 of acclimatization was the same as day 1 except that the top speed was 12m/min for 5 minutes. During testing day, mice were placed in the treadmill at an elevation of 10°, and the treadmill belt speed was increased stepwise over time, to a maximum of 26m/min (Figure 2F). Mice were considered fatigued if they entered the fatigue zone for more than 5 seconds in 3 separate instances and were subsequently removed from the treadmill. Blood was collected immediately after the mice were removed from the treadmill, and lactate levels were assayed using the Lactate Plus Meter (Nova Biomedical) according to the manufacturer's instructions. Work done was calculated by the following: *total distance traveled (m) * body weight (kg) * standard gravity (m/s^2) * sin(10°)*.

2.4. Gene expression quantification by qPCR

RNA was isolated by phenol-chloroform extraction from whole blood and homogenized brain tissue, followed by cDNA synthesis for qPCR reactions and analysis as previously described (Aw et al., 2020). Gene expression was normalized to *Hprt1* and compared using the $\Delta\Delta C_t$ method. The ISG index by sample was calculated by taking the

geometric mean of the normalized expression values of all 5 ISGs. qPCR primers were as follows:

Hprt1 (F: 5'-GCGTCGTGATTAGCGATGATG, R: 5'-CTCGAGCAAGTCTTTCAGTCC); *Mx1* (F: 5'-CAGCAGTTCAGTCCCATAAC, R: 5'-GACTATAGCTGCTGGTTGTATG); *Ifit3* (F: 5'-TCATGAGTGAGGTCAACCGGG, R: 5'-TGGTTGCACACCCTGTCTTC); *Oas2* (F: 5'-GAAACTTCATTCAAACCCGGCCCA, R: 5'-CCGGAAGCCTTCAGCAATGTCAAA); *Isg15* (F: 5'-GGCCACAGCAACATCTATGA, R: 5'-CGCAAATGCTTGATCACTGT); *Rsad2* (F: 5' TGCTGGCTGAGAATAGCATTAGG, R: 5'-GCTGAGTGCTGTTCCCATCT).

2.5. Genotyping

Genotyping was performed using the primers indicated in Supplementary Table 1.

2.6. Histology

Mouse tissue was dissected and fixed in 4% PFA (Electron Microscopy Sciences) before delivery to the Dana Farber/Harvard Cancer Center (DF/HCC) rodent histopathology core facility for further processing. Samples were embedded in paraffin, sectioned, and stained using hematoxylin and eosin by the core facility. 2 sections per tissue per subject were analyzed in a single-blind manner by an experienced pathologist at the core facility. Images were captured using an IX70 bright field microscope (Olympus) at 10X magnification.

2.7. Multiplexed Error Robust Fluorescent In-Situ Hybridization (MERFISH) and analysis

The full list of MERFISH probes is indicated in Supplementary Table 2. Probe design, sample staining, imaging, imaging analysis, and cell segmentation protocols have been described previously (Moffitt et al., 2018). MERFISH probe sequences were designed using reference transcriptomic data from the Ensembl Genome Reference Consortium Mouse Build 38 (mm10). "Pan" versions of murine *Ifna* and *Ifnl* were designed by selecting probe sequences that bind to multiple family members of each gene (allowing for 1nt mismatch), such that each gene had between 60 and 70 cognate probes. Quality control metrics for a representative B6 and *Sle1,Yaa* dataset are reported in Supplementary Figure 7, with per sample metadata reported in Supplementary Table 3.

Cellular, RNA count, and spatial metadata obtained after MERFISH imaging and decoding were incorporated into the Anndata format, then filtered for cellular features and RNA counts and normalized by cell volume prior to concatenation and downstream analysis using the Scanpy package (v1.8.2) (Wolf et al., 2018). Cells were further filtered at this stage by counts (>20 and <2000) and genes (>2) prior to the application of standard dimensional reduction and clustering workflows. Differential gene expression was performed using the Wilcoxon rank-sum test, and the Benjamini-Hochberg method for multiple testing correction was used, as implemented in the Scanpy package.

2.8. RNAscope in situ hybridization and analysis

Mouse brains were dissected following terminal anesthesia and transcardial perfusion of 20mL ice-cold PBS. RNAscope *in situ* hybridization was performed on 16μm thick cryosections as previously described (Aw et al., 2020) using probes directed against *Ifit3* (508251, ACD Bio) according to the manufacturer's instructions. Confocal images

were obtained at either 10X or 30X magnification using the FV3000 confocal system (Olympus). Stitching of tiled images was performed on the Fluoview FV3000 software (Olympus).

2.9. Serum ELISA for murine cytokines

Serum samples were assayed on the VeriPlex Mouse Cytokine 9-Plex ELISA Kit (PBL Assay Science) by contract service from the company (PBL Assay Science).

2.10. Single-nucleus sequencing (sNucSeq) and analysis

The protocol for single-nucleus isolation was adapted from previous studies (Habib et al., 2016, 2017). Briefly, brain regions (hindbrain and whole hippocampus) were dissected and snap frozen on dry ice after mice were transcardially perfused with 20mL ice-cold PBS. The tissue was dounce homogenized in 2mL ice-cold nuclei EZ Prep buffer (Sigma), washed, and resuspended in ice-cold NSB (1% BSA, 0.1% RNase inhibitor in 1X RNase free PBS). Nuclei were stained with eFluor-780 (eBioscience) on ice, washed, and FACS-sorted (BD FACSAria) through a 70μm nozzle in "Purity" mode. An aliquot of nuclei was stained with 0.4% trypan blue (Sigma) and counted in a hemacytometer (VWR Scientific). The appropriate concentration of viable nuclei for a target nuclei number (5000) per sample lane was then used as input for the Chromium NextGem Single Cell 3' GEM, Library & Gel Bead Kit v3.1 (10X Genomics) following the manufacturer's instructions. Samples were pooled equimolarly, and sequencing was performed on a NovaSeq 6000 sequencer (Illumina) with 1pM input on an S4 flow cell. Sequencing output files were demultiplexed, aligned to a reference genome, and single-cell counts were generated using the cellranger (v5.0.0, 10X Genomics) pipeline with parameters optimized for nuclei samples as recommended by the manufacturer.

Individual datasets from each 10X chip sample lane were first filtered for genes and cells with a minimum value threshold (min.cells=3, min.features=200), followed by a second round of filtering for minimum RNA counts (>3000), gene number (>1000 and <7500), and mitochondrial content (<5). Post-quality control metrics are reported in Supplementary Table 4.

Read counts were then normalized and variance-stabilized using the sctransform package (Hafemeister and Satija, 2019) prior to integration and standard downstream analysis with the Seurat v3 package (Stuart et al., 2019). Differential expression testing was performed using the DESingle package (Miao et al., 2018). Gene ontology analysis was performed using the gProfiler2 package (Raudvere et al., 2019). Receptor-ligand analysis was performed using the Squidpy package's (Palla et al., 2021) implementation of permutation testing originally described in the CellPhone DB package (Efremova et al., 2020).

2.11. Statistical analysis

For all statistical analyses, R and GraphPad Prism 8 (GraphPad Software) were used. Error bars represent the standard deviation (s.d.) in all figures. All replicate numbers, statistical tests, p values, and q values used are indicated in the figure legends where appropriate. Statistical tests were selected based on the normality of the data distribution, as assessed by the Shapiro-Wilk test or quantile-quantile (QQ) plot, and on the equality of variance, as assessed by the F test. For comparisons across multiple groups, the appropriate ANOVA tests were used, and the resultant pairwise comparisons were corrected for multiple testing. The specific tests used are indicated in

the figure legends where appropriate. Sample sizes and power were not estimated using any statistical methods.

3. Results

3.1. Peripheral correlates of autoimmunity reach peak expression by 14 weeks in *Sle1,Yaa* males.

An enhanced ISG signature is frequently observed in the peripheral blood of lupus patients, with the enrichment of ISG-high cell types correlating with disease severity (Banchereau et al., 2016; Nehar-Belaid et al., 2020). Various murine models of lupus express different intensities of the type 1 interferon gene signature (Zhuang et al., 2015). However, granular temporal data on how these gene expression signatures develop longitudinally remain sparse. Thus, we determined the kinetics of the peripheral blood ISG signature by assessing the aggregate gene expression of a 5-ISG panel (*Mx1*, *Ifit3*, *Oas2*, *Isg15*, *Rsad2*) in serially bled B6 and *Sle1,Yaa* mice. These genes were selected because their human orthologues are enriched in PBMC transcripts from lupus patients across multiple studies (Baechler et al., 2003; Banchereau et al., 2016; Bennett et al., 2003). While the temporal trajectory of individual genes was variable, they all reached peak expression at about 14 weeks of age (Supplemental Figure 1A). These gene-level differences could be due to changes in cell type composition or to modulatory signaling events from other cytokines. Interestingly, we also observed an age-dependent increase in serum TNFα, decreased serum CCL5, and trends toward increased serum IL-6 and IL-10 in *Sle1,Yaa* mice (Supplementary Figure 1B).

In aggregate, the ISG signature peaked at 14 weeks of age in *Sle1,Yaa* mice then decreased until at least 20 weeks of age (Figure 1A). IFNα is thought to be the

predominant interferon responsible for the heightened type 1 interferon signature observed in SLE patients (Crow, 2016; Hua et al., 2006). However, we did not observe statistically significant differences in serum IFNα between genotypes and age groups (Figure 1B), although there was a trend toward higher levels in 14-week and 20-week-old *Sle1,Yaa* mice. Given known difficulties in measuring serum IFNα levels, we speculate that the development of higher sensitivity techniques could unmask differences. A similar temporal trend was observed in autoantibody titers, where an aggregated autoantibody score comprising 19 autoantigens peaked at 14 weeks of age but appeared to level off at 20 weeks of age (Figure 1C and Supplementary Figure 1C). Collectively, these observations suggest that key peripheral blood autoimmune correlates in the *Sle1,Yaa* lupus mouse model begin developing by 8 weeks of age and reach a peak at 14 weeks of age, before diverging by 20 weeks of age.

3.2. *Sle1,Yaa* mice exhibit anxiety- and fatigue-like behavioral phenotypes.

We hypothesized that any type 1 interferon signaling-dependent behavioral phenotypes would correlate with proxy measures of the peripheral blood ISG signature. Consequently, we performed behavioral phenotyping at the 14-week timepoint, when peak type 1 interferon signature was observed. A pilot battery of behavioral tests did not reveal any social-, cognitive-, or depressive-like phenotypes, but suggested anxiety- and fatigue-like phenotypes (data not shown), which are found in 37% and 80% of NPSLE patients, respectively (Ahn and Ramsey-Goldman, 2012; Zhang et al., 2017). Using an expanded battery of behavioral tests for anxiety- and fatigue-like phenotypes, we confirmed that *Sle1,Yaa* mice displayed increased anxiety- (Figure 2A – 2B; Supplementary Figure 2A) and fatigue-like behaviors (Figure 2C – 2F; Supplementary

Figure 2B). Gait analyses did not reveal any statistically significant differences in motor coordination between B6 and *Sle1,Yaa* mice (Supplementary Figure 2C), and gross pathology was not observed in major joint or muscular tissues from B6 or *Sle1,Yaa* mice (Supplementary Figure 2D), suggesting that fatigue, not ataxia or peripheral tissue inflammation or damage, is the main contributor to the decreased locomotive phenotypes observed. These anxiety- and fatigue-like behaviors also persisted at 20 weeks of age despite the altered cytokine and type 1 interferon signature profile present at this age in *Sle1,Yaa* mice (Supplementary Figure 3), suggesting a potential decoupling between peripheral inflammation and behavioral phenotypes.

Maternal inflammation and genetic drift contribute to rodent behavioral phenotypes (Aw et al., 2021; Crusio et al., 2009). Due to the location of the *Yaa* mutation on the Y chromosome, gender-matched littermates could not be used to control for the aforementioned factors. Therefore, we utilized a breeding scheme (Supplementary Figure 4A) where subjects were derived from *Sle1* heterozygous dams that were themselves derived from crosses between *B6* and *Sle1,Yaa* mice (complex breeders). Because pups were derived from dams with the same genotype, maternal inflammation could be controlled. The effect of genetic drift was minimized by using breeder mice that were derived from multiple crosses between the 2 genotypes. The fold change increase in the peripheral blood ISG signature in 14-week complex breeder–derived *Sle1,Yaa* mice was comparable to that of normal breeder–derived *Sle1,Yaa* mice (Supplementary Figure 4B). In comparing the behavioral phenotypes of complex breeders with normal breeders, we also found that genotype, but not breeding, accounted for most of the variance observed except for grip strength, where both genotype and breeding

accounted for similar levels of variance (Supplementary Figure 4C-J). These results suggest that contributions from maternal inflammation and genetic drift to both peripheral autoimmunity and behavior are minimal and that genotype is the largest explanatory factor for the observed phenotypes. Therefore, we utilized homozygously bred mice for all other experiments.

3.3. Unbiased single-nucleus sequencing confirms the dominant upregulation of type 1 interferon signaling and reveals a general decrease in cellular and synaptic interactions.

Using spatial transcriptomic techniques which are described further in **Section 3.4**, we prescreened brain regions which display (1) a relatively high degree and consistency of ISG enrichment and (2) evidence of anatomical correlation with our observed behavioral phenotypes of anxiety- and fatigue-like behavior. We leveraged unbiased single-nuclei sequencing (sNucSeq, Habib et al., 2016, 2017) on the whole (dorsal and ventral) hippocampus (Arriaga and Han, 2017; Jimenez et al., 2018) and hindbrain (Barnden et al., 2011; Venkatraman et al., 2017) of 14-week-old B6 and *Sle1,Yaa* mice (N=2 per genotype). After quality control filtering and separate concatenation of the hindbrain and hippocampal datasets, 33327 cells with 2639 median genes per cell and 7403 median UMI counts per cell and 31005 cells with 4414 median genes per cell and 17441 median UMI counts per cell were retained, respectively, from B6 or *Sle1,Yaa* mice (Supplementary Figure 5A and Supplementary Table 4).

We identified the expected major cell classes in each of the datasets (Figure 3A; Supplementary Figure 5B and 5C), with similar clustering patterns across individual samples and genotypes (Supplementary Figure 5D and 5E). Enrichment of the ISG

index was apparent in vascular and glial cell types in both the hindbrain and hippocampus within the *Sle1,Yaa* genotype. Interestingly, there also appeared to be a small ISG signature–enriched population in the *Sle1,Yaa* hippocampal dentate gyrus (DG) and CA3 cell types (Figure 3B and 3C). Due to the low numbers of nuclei obtained for the vascular, polydendrocyte, and microglia cell classes, and the low proportion of neurons expressing ISGs, we focused our analyses on the other glial cell types (astrocytes and oligodendrocytes) that make up the bulk of the ISG expressing cluster of cells.

We first confirmed that ISGs accounted for most of the differentially expressed genes between genotypes in both brain regions (Figure 3D), supporting the hypothesis that dysregulated type 1 interferon signaling is a key driver of pathology in the *Sle1,Yaa* brain. Narrowing down to astrocytes and oligodendrocytes, ISGs still remained the predominant class of differentially expressed genes (DEGs), accounting for >50% DEGs in both the hindbrain and hippocampus (Supplementary Figure 6A and 6B). Pathway analyses of differentially expressed genes within astrocytes from both brain regions showed an expected upregulation of the type 1 interferon response pathway. Also interestingly, our analyses show asymmetric downregulation of biological pathways between brain regions: nervous system development and neurogenesis terms were downregulated only in hindbrain astrocytes and the lipid metabolism term was downregulated only in hippocampal astrocytes, suggesting regional differences in the biological response to IFNα among astrocytes (Supplementary Figure 6C and 6D). Cholesterol synthesis and secretion by hippocampal astrocytes is critical for synaptic maturation and, consequently, for short- and long-term potentiation in neurons (van

Deijk et al., 2017); it could therefore be of interest to further investigate the role of perturbed astrocyte lipid metabolism on neuronal function in *Sle1,Yaa* mice.

Interestingly, despite the high proportion of ISG DEGs in oligodendrocytes, only the hippocampal oligodendrocytes had strongly upregulated antiviral/type 1 interferon– related pathways, once again reflecting a possible region-specific difference in the cellular response to IFNα signaling. Conversely, hindbrain oligodendrocytes had stronger upregulation of multiple metabolic pathways, including nitrogen metabolism and oxidative phosphorylation (OXPHOS). Oligodendrocytes from both brain regions had a general downregulation of neuronal developmental and synaptic interaction pathways (Supplementary Figure 6E and 6F), suggesting they had fewer interactions with other CNS cell types. This is another interesting avenue of further investigation, as cellular interactions between oligodendrocytes and neurons are necessary for targeted axon myelination (Almeida, 2018). In fact, NPSLE patients tend to have white matter abnormalities (Costallat et al., 2018; Jung et al., 2010), suggesting a clear clinical phenotype that may be replicated in the *Sle1,Yaa* mouse model.

Given the enrichment of ISGs across these regions, as well as the spatial clustering of these cells (refer to results in **Section 3.4**), we arbitrarily defined a subset of cells that highly express ISGs and queried their potential interactions between astrocytes, oligodendrocytes, and major neuronal clusters with all other cell types within this subset using Squidpy's ligand-receptor analysis package (Palla et al., 2021). We prioritized interaction factors with source cell types containing genes that were previously defined as differentially expressed and found a general decrease in cellular and synaptic interaction pathways. By querying the Interferome database (Rusinova et al., 2013),

some of these interaction factor genes were also identified as ISGs (e.g. *Nlgn1*, *Nlgn2*) or negatively regulated by type 1 interferon signaling (e.g. *Nrxn3*, *Fgf14*), suggesting that particular interactions may in fact be enriched, or repressed, within the ISG patches relative to the non-ISG milieu. We observe an almost uniform decrease in components of the type 1 interferon-regulated Neuroligin (*Nlgn*) – Neurexin (*Nrxn*) synapse adhesion module across hindbrain astrocytes, hippocampal oligodendrocytes, and most major neuronal clusters, with the exception of the Excitatory Neuron 1 cluster in the hindbrain, and the DG cluster in the hippocampus (Supplementary Figure 7, Supplementary Tables 5 and 6). We also found a universal decrease in the expression of *Fgf12* and *Fgf14* among the major neuronal classes. FGF12 and FGF14 physically interact with voltage-gated sodium channels and regulate action potential transmission (Pablo et al., 2016). Interestingly, *Fgf14* knockout (*Fhf4$^{-/-}$*) and *Fgf12*, *Fgf14* double knockout (*Fhf1$^{-/-}$*, *Fhf4$^{-/-}$*) mice showed clear evidence of ataxia and motor weakness, which was attributed to decreased intrinsic excitability of cerebellar granule neurons (Goldfarb et al., 2007).

The overall downregulation of cellular communication interactions in these cell types across brain regions of *Sle1,Yaa* mice suggests that neurons have fewer interactions with each other, astrocytes, and oligodendrocytes within this type 1 interferon inflammation milieu. Given the multifaceted roles of glial-neuron synaptic communication in maintaining neuronal homeostasis, particularly with respect to astrocytes (Mederos et al., 2018), it will be important to further define key dysregulated interaction factors between these cell types and interrogate their possible roles in mediating behavioral phenotypes in *Sle1,Yaa* mice.

3.4. The type 1 interferon signature is spatially enriched within the brain parenchyma of *Sle1,Yaa* mice.

Given the varying functions across regions of the brain, we hypothesized that spatial specificity in ISG enrichment could underlie differences in behavior. Leveraging the multiplexed error-robust fluorescence in situ hybridization (MERFISH) (Chen et al., 2015), we designed a 224-plex gene library that included a curated panel of 58 ISGs that impact other cellular processes, such as metabolism and transcription, and that were highly conserved across different animal phylogenies (Shaw et al., 2017) (Supplementary Table 2). Other gene sets included broad cell type markers and genes involved in neuronal activation and phagocytic engulfment. These genes were selected to reflect the known roles of type 1 interferon in modulating neuronal firing rates and increasing microglial synaptic engulfment, both of which influence behavioral outcomes (Blank et al., 2016; Dafny et al., 1996; Reyes-Vazquez et al., 1982; Aw et al., 2020; Roy et al., 2020). A selection of cytokines (including pan-*Ifna* and pan-*Ifnl*) and chemokines were also included to leverage the greater sensitivity of FISH-based approaches in detecting short genes, which have higher dropout rates in single-cell sequencing approaches (Phipson et al., 2017). Given the clear behavioral phenotypes observed at 14 weeks of age, we performed MERFISH on 2 biological replicates each of 14-week-old *Sle1,Yaa* and B6 controls.

In total, we profiled >400,000 cells with a total RNA count of ~197 million across the 4 samples (Supplementary Table 3 and Supplementary Figure 8) and identified all major cell classes present in the brain (Figures 4A), in their expected spatial distribution (Supplementary Figure 9A). We identified a subset of the ISG gene set that appeared to

be enriched in aggregate within the vascular and glial cell classes of *Sle1,Yaa* mice (Figure 4B). Strikingly, these ISGs appeared to be spatially segregated into distinct patches across the brain parenchyma (Figure 4C), with distinct spatial "ranges" across different ISGs (Supplementary Figure 9B). The presence of these ISG patches was independently validated using RNAscope *in situ* hybridization, which showed spatially heterogeneous localizations across the brain parenchyma that appear to be more prevalent in the subcortical regions (Figure 4D). Interestingly, these patches also appeared to be present at both 8 weeks and 20 weeks of age (Supplementary Figure 10), suggesting that type 1 interferon-mediated inflammation in the brain could predate overt peripheral autoimmune inflammation and that it persists despite changes in the peripheral blood interferon signature.

In summary, our transcriptomic data collectively suggest that dysregulated IFNAR signaling is a key event within the CNS of *Sle1,Yaa* mice that is spatially restricted and more enriched in glial cells compared to neurons. Despite brain region-specific differences in other affected cellular pathways, there appeared to be a uniform cellular response to type 1 interferon signaling, as well as a concomitant decrease in cellular and synaptic interactions among most clusters. We therefore hypothesize that CNS-restricted IFNAR signaling plays a key mechanistic role in mediating the behavioral phenotypes we observed in the *Sle1,Yaa* mice, perhaps by modulating cellular and synaptic interactions between CNS cell types, and that therapeutic blockade of IFNAR signaling in the CNS can rescue behavioral deficits.

4. Discussion

In the *Sle1,Yaa* mouse model of lupus, which develops accelerated autoimmune disease due to over-exuberant TLR7 signaling, we found that an elevated peripheral blood type 1 interferon signature appears at 8 weeks of age, peaks at 14 weeks of age, and declines by 20 weeks of age. This observation could be due to the differential expression of cytokines, most notably TNFα (Supplementary Figure 1A), which can repress type 1 interferon signaling but also independently induce a subset of ISGs (Cantaert et al., 2010; Wang et al., 2016). Elevated TNFα levels are also observed in SLE patients and correlate strongly with renal disease activity (Idborg et al., 2018). Furthermore, serum autoantibody titers in the *Sle1,Yaa* model show a similar trend, being slightly elevated at 8 weeks of age, prior to peaking at 14 and 20 weeks of age (Supplementary Figure 1B). The *Sle1,Yaa* mouse model therefore exhibits an accelerated lupus-like autoimmune disease that recapitulates key immunological features of human disease. Importantly, we found that the *Sle1,Yaa* mouse model displays anxiety- and fatigue-like behavioral deficits that are reflective of common neuropsychiatric symptoms experienced by NPSLE patients (Ahn and Ramsey-Goldman, 2012; Zhang et al., 2017) and may be linked to ISG-enriched patches in the brain.

Our findings raise important questions about the source of type 1 interferon stimulating the formation of these ISG patches and how the patches lead to behavioral phenotypes. The patch-like nature of ISGs argues against a model of peripheral type 1 interferons randomly crossing the blood-brain barrier. Since CNS blood vessels are IFNAR-signaling competent and the first point of CNS contact from circulating cytokines, a peripheral source of IFNα would be expected to result in ISG positivity across the brain

vasculature, which was not observed. Moreover, our preliminary experiments with B6-*Sle1,Yaa* parabiotic mice and peripherally injected IFNα do not show evidence of ISG patch formation (Aw et al 2020; E.A., unpublished data). Given low levels of circulating peripheral blood IFNα in SLE patients (Rodero et al., 2017), it is likely that peripherally produced type 1 interferons in lupus are largely consumed by a peripheral "sink", leaving insignificant amounts to cross the blood-brain barrier, which already possesses limited permeability to IFNα (Pan et al., 1997). However, we cannot discount the possibility of immune cells that circulate to the meninges early in life or those derived from the calvarial bone marrow as sources of local type 1 interferon (Brioschi et al., 2021; Cugurra et al., 2021). Another possibility is intracerebroventricular (ICV) production of IFNα, which has been detected in the cerebrospinal fluid (CSF) of NPSLE patients (Shiozawa et al., 1992; Varley et al., 2020). While this could be a potential source during the later course of disease, it is unlikely prior to the 20-week timepoint in *Sle1,Yaa* mice, given that ISG expression was not apparent among ependymal cells in either of our sequencing or *in situ* hybridization data.

Another possibility would be brain parenchyma-derived type 1 interferon; *Tlr7* is most abundantly expressed by microglia within the CNS (Michaelis et al., 2019), and the *Yaa* allele-mediated *Tlr7* could enhance signaling and endogenous production of type 1 interferons and other inflammatory cytokines. Consequently, the observations of ISG patches could result from stochastic activation of TLR7 signaling by individual microglia, leading to geographically restricted areas of inflammation. While our MERFISH data show small but statistically significant differences in some microglial cytokine expression, they were not spatially enriched. Moreover, we did not detect any

transcriptional enrichment of microglial cytokines within our sNucSeq dataset. Therefore, much remains to be uncovered regarding the source of inflammatory cytokines driving the formation of CNS ISG patches, and as a corollary, their temporal persistence within defined geographies.

Among ISG patches, our sNucSeq pathway analysis demonstrated a general downregulation of synaptic adhesion components (e.g. *Nlgn1, Nlgn2, Lrfn5*) in several neuronal clusters. These synaptic adhesion molecules play a key role in synaptic maturation and organization, and show strong genome-wide associations with several neuropsychiatric diseases (Lie et al., 2018; Südhof, 2017). However, in the hindbrain, these interaction factors were contrarily enriched in pairings between the Serotonergic Neuron cluster with clusters of Excitatory Neuron 2, Excitatory Neuron 3, and Interneuron. Serotonin plays a critical role in mediating higher-order behaviors, especially the anxiety- and fatigue-like behaviors we observe in *Sle1,Yaa* mice (Fischer and Ullsperger, 2017; Marcinkiewcz et al., 2016). The altered connectivity between the raphe nuclei (main producers of serotonin, located in the hindbrain) and their afferent inputs could therefore result in dysregulated serotonergic neurotransmission, thereby affecting behavior.

In summary, while all cell types within the CNS parenchyma can respond to type 1 interferon, it is unlikely that any one cell type will singularly be sufficient to cause behavioral pathology in the *Sle1,Yaa* model. It will be important to systematically dissect the contributions of individual CNS cell types, within and outside the ISG patches, to behavioral phenotypes in the *Sle1,Yaa* model.

5. Study limitations and future directions.

A key limitation of our study is that the *Yaa*-driven male bias in the *Sle1,Yaa* model does not reflect the overwhelming female (9 to 1) bias in human disease (Tsokos, 2011). However, genetic polymorphisms and copy number variations in the TLR7 signaling pathway, as well as in T and B cell signaling, have been identified as risk factors for SLE (Moulton et al., 2017). Furthermore, there is 14-fold increased risk of SLE in male Klinefelter's syndrome (XXY chromosome configuration) patients (Scofield et al., 2008). These human genetic studies suggest that the immunological basis of the *Sle1,Yaa* mouse model is relevant to human disease despite the incongruency in gender bias. The *Sle1,Tg7* mouse is a modified version of *Sle1,Yaa* that could address this gender limitation. Instead of *Yaa*, *Sle1,Tg7* contains a transgenic *Tlr7* without the flanking genes in *Yaa*, mirroring the two-fold increase in expression of *Tlr7* as well as autoimmune sequelae seen in *Sle1,Yaa* male mice (Hwang et al., 2012). Thus, the *Sle1,Tg7* strain would likely be a viable alternative that better reflects the gender bias seen in human patients, given that the *Tg7* transgene is present on an autosomal chromosome, and female *Sle1,Tg7* can therefore be experimentally prioritized.

In order to test the necessity of the *Sle1,Yaa* genetic background in the CNS parenchyma in generating ISG patches, we have planned to perform B6 and *Sle1,Yaa* bone marrow transfers into irradiated *Ifnar1*-sufficient and deficient *Sle1,Yaa* recipients.

Finally, a key next step in terms of human translatability would involve validation of the type 1 interferon signature in the brains of NPSLE patients, as well as the possibility of the interferon signature being spatially restricted in patches *vis-a-vis* the *Sle1,Yaa* mouse brain.

6. Conclusions

Our work lays the foundation for further investigation of CNS IFNAR signaling in NPSLE. We demonstrate that the *Sle1,Yaa* mouse model of NPSLE exhibits spatially enriched patches of ISGs in the brain and that the type 1 interferon signature is a dominantly upregulated pathway in the brain. A greater understanding of the mechanistic link between the spatially restricted interferon signaling and subsequent behavior changes will support the potential therapeutic use and development of blood brain barrier–permeable type 1 interferon signaling modulators for NPSLE.

7. References

Ahn, G.E., and Ramsey-Goldman, R. (2012). Fatigue in systemic lupus erythematosus. Int. J. Clin. Rheumtol. *7*, 217–227.

Almeida, R.G. (2018). The Rules of Attraction in Central Nervous System Myelination. Front. Cell. Neurosci. *12*.

Arriaga, M., and Han, E.B. (2017). Dedicated hippocampal inhibitory networks for locomotion and immobility. J. Neurosci. *37*, 9222–9238.

Aw, E., Zhang, Y., and Carroll, M. (2020). Microglial responses to peripheral type 1 interferon. J. Neuroinflammation *17*, 340.

Aw, E., Zhang, Y., Yalcin, E., Herrmann, U.S., and Carroll, M.C. (2021). Neuropsychiatric disorders: An immunological perspective. In Advances in Immunology, pp. 83–155.

Baechler, E.C., Batliwalla, F.M., Karypis, G., Gaffney, P.M., Ortmann, W.A., Espe, K.J., Shark, K.B., Grande, W.J., Hughes, K.M., Kapur, V., et al. (2003). Interferon-inducible gene expression signature in peripheral blood cells of patients with severe lupus. Proc. Natl. Acad. Sci. U. S. A. *100*, 2610–2615.

bioRxiv preprint doi: https://doi.org/10.1101/2023.04.21.537814; this version posted April 21, 2023. The copyright holder for this preprint (which was not certified by peer review) is the author/funder, who has granted bioRxiv a license to display the preprint in perpetuity. It is made available under aCC-BY-NC-ND 4.0 International license.

Banchereau, R., Hong, S., Cantarel, B., Baldwin, N., Baisch, J., Edens, M., Cepika, A.-M., Acs, P., Turner, J., Anguiano, E., et al. (2016). Personalized Immunomonitoring Uncovers Molecular Networks that Stratify Lupus Patients. Cell *165*, 551–565.

Barnden, L.R., Crouch, B., Kwiatek, R., Burnet, R., Mernone, A., Chryssidis, S., Scroop, G., and del Fante, P. (2011). A brain MRI study of chronic fatigue syndrome: Evidence of brainstem dysfunction and altered homeostasis. NMR Biomed. *24*, 1302–1312.

Bennett, L., Palucka, A.K., Arce, E., Cantrell, V., Borvak, J., Banchereau, J., and Pascual, V. (2003). Interferon and granulopoiesis signatures in systemic lupus erythematosus blood. J. Exp. Med. *197*, 711–723.

Blank, T., Detje, C.N., Spieß, A., Hagemeyer, N., Brendecke, S.M., Wolfart, J., Staszewski, O., Zöller, T., Papageorgiou, I., Schneider, J., et al. (2016). Brain Endothelial- and Epithelial-Specific Interferon Receptor Chain 1 Drives Virus-Induced Sickness Behavior and Cognitive Impairment. Immunity *44*, 901–912.

Brioschi, S., Wang, W.-L., Peng, V., Wang, M., Shchukina, I., Greenberg, Z.J., Bando, J.K., Jaeger, N., Czepielewski, R.S., Swain, A., et al. (2021). Heterogeneity of meningeal B cells reveals a lymphopoietic niche at the CNS borders. Science (80-.). *373*, eabf9277.

Cantaert, T., Baeten, D., Tak, P.P., and van Baarsen, L.G. (2010). Type I IFN and TNFα cross-regulation in immune-mediated inflammatory disease: basic concepts and clinical relevance. Arthritis Res. Ther. *12*, 219.

Chen, K.H., Boettiger, A.N., Moffitt, J.R., Wang, S., and Zhuang, X. (2015). Spatially resolved, highly multiplexed RNA profiling in single cells. Science (80-.). *348*, 1360–1363.

Costallat, B.L., Ferreira, D.M., Lapa, A.T., Rittner, L., Costallat, L.T.L., and Appenzeller, S. (2018). Brain diffusion tensor MRI in systematic lupus erythematosus: A systematic review. Autoimmun. Rev. *17*, 36–43.

Crow, M.K. (2014). Type I Interferon in the Pathogenesis of Lupus. J. Immunol. 192, 5459–5468.

Crow, M.K. (2016). Interferon α or β: which is the culprit in autoimmune disease? Nat. Rev. Rheumatol. *12*, 439–440.

Crusio, W.E., Goldowitz, D., Holmes, A., and Wolfer, D. (2009). Standards for the publication of mouse mutant studies. Genes, Brain Behav. *8*, 1–4.

Cugurra, A., Mamuladze, T., Rustenhoven, J., Dykstra, T., Beroshvili, G., Greenberg, Z.J., Baker, W., Papadopoulos, Z., Drieu, A., Blackburn, S., et al. (2021). Skull and vertebral bone marrow are myeloid cell reservoirs for the meninges and CNS parenchyma. Science (80-.). *373*.

Dafny, N., Prieto-Gomez, B., Dong, W.Q., and Reyes-Vazquez, C. (1996). Interferon modulates neuronal activity recorded from the hypothalamus, thalamus, hippocampus, amygdala and the somatosensory cortex. Brain Res. *734*, 269–274.

Das, A., Heesters, B.A., Bialas, A., Carlesso, G., Herbst, R., and Carroll, M.C. (2017). Follicular Dendritic Cell Activation by TLR Ligands Promotes Autoreactive B Cell Responses. Immunity *46*, 106–119.

van Deijk, A.L.F., Camargo, N., Timmerman, J., Heistek, T., Brouwers, J.F., Mogavero, F., Mansvelder, H.D., Smit, A.B., and Verheijen, M.H.G. (2017). Astrocyte lipid metabolism is critical for synapse development and function in vivo. Glia *65*, 670–682.

Dougherty, J.P., Springer, D.A., and Gershengorn, M.C. (2016). The Treadmill Fatigue

Test: A Simple, High-throughput Assay of Fatigue-like Behavior for the Mouse. J. Vis. Exp.

Efremova, M., Vento-Tormo, M., Teichmann, S.A., and Vento-Tormo, R. (2020). CellPhoneDB: inferring cell–cell communication from combined expression of multi-subunit ligand–receptor complexes. Nat. Protoc. *15*, 1484–1506.

Fairhurst, A.M., Hwang, S.H., Wang, A., Tian, X.H., Boudreaux, C., Zhou, X.J., Casco, J., Li, Q.Z., Connolly, J.E., and Wakeland, E.K. (2008). Yaa autoimmune phenotypes are conferred by overexpression of TLR7. Eur. J. Immunol. *38*, 1971–1978.

Fischer, A.G., and Ullsperger, M. (2017). An Update on the Role of Serotonin and its Interplay with Dopamine for Reward. Front. Hum. Neurosci. *11*.

Goldfarb, M., Schoorlemmer, J., Williams, A., Diwakar, S., Wang, Q., Huang, X., Giza, J., Tchetchik, D., Kelley, K., Vega, A., et al. (2007). Fibroblast Growth Factor Homologous Factors Control Neuronal Excitability through Modulation of Voltage-Gated Sodium Channels. Neuron *55*, 449–463.

Habib, N., Li, Y., Heidenreich, M., Swiech, L., Avraham-Davidi, I., Trombetta, J.J., Hession, C., Zhang, F., and Regev, A. (2016). Div-Seq: Single-nucleus RNA-Seq reveals dynamics of rare adult newborn neurons. Science (80-.). *353*, 925–928.

Habib, N., Avraham-Davidi, I., Basu, A., Burks, T., Shekhar, K., Hofree, M., Choudhury, S.R., Aguet, F., Gelfand, E., Ardlie, K., et al. (2017). Massively parallel single-nucleus RNA-seq with DroNc-seq. Nat. Methods *14*, 955–958.

Hafemeister, C., and Satija, R. (2019). Normalization and variance stabilization of single-cell RNA-seq data using regularized negative binomial regression. Genome Biol. *20*, 296.

Hua, J., Kirou, K., Lee, C., and Crow, M.K. (2006). Functional assay of type I interferon in systemic lupus erythematosus plasma and association with anti–RNA binding protein autoantibodies. Arthritis Rheum. *54*, 1906–1916.

Hwang, S.-H., Lee, H., Yamamoto, M., Jones, L.A., Dayalan, J., Hopkins, R., Zhou, X.J., Yarovinsky, F., Connolly, J.E., Curotto de Lafaille, M.A., et al. (2012). B Cell TLR7 Expression Drives Anti-RNA Autoantibody Production and Exacerbates Disease in Systemic Lupus Erythematosus–Prone Mice. J. Immunol. *189*, 5786–5796.

Idborg, H., Eketjäll, S., Pettersson, S., Gustafsson, J.T., Zickert, A., Kvarnström, M., Oke, V., Jakobsson, P.-J., Gunnarsson, I., and Svenungsson, E. (2018). TNF-α and plasma albumin as biomarkers of disease activity in systemic lupus erythematosus. Lupus Sci. Med. *5*, e000260.

Jimenez, J.C., Su, K., Goldberg, A.R., Luna, V.M., Biane, J.S., Ordek, G., Zhou, P., Ong, S.K., Wright, M.A., Zweifel, L., et al. (2018). Anxiety Cells in a Hippocampal-Hypothalamic Circuit. Neuron *97*, 670-683.e6.

Jeltsch-David, H., and Muller, S. (2014). Neuropsychiatric systemic lupus erythematosus: Pathogenesis and biomarkers. Nat. Rev. Neurol. *10*, 579–596.

El Khoury, L., Zarfeshani, A., and Diamond, B. (2020). Using the Mouse to Model Human Diseases: Cognitive Impairment in Systemic Lupus Erythematosus. J. Rheumatol. *47*, 1145–1149.

Jung, R.E., Caprihan, A., Chavez, R.S., Flores, R.A., Sharrar, J., Qualls, C.R., Sibbitt, W., and Roldan, C.A. (2010). Diffusion tensor imaging in neuropsychiatric systemic lupus erythematosus. BMC Neurol. *10*.

Kivity, S., Agmon-Levin, N., Zandman-Goddard, G., Chapman, J., and Shoenfeld, Y.

(2015). Neuropsychiatric lupus: A mosaic of clinical presentations. BMC Med. *13*, 1–11.

Lie, E., Li, Y., Kim, R., and Kim, E. (2018). SALM/Lrfn Family Synaptic Adhesion Molecules. Front. Mol. Neurosci. *11*.

Lisnevskaia, L., Murphy, G., and Isenberg, D. (2014). Systemic lupus erythematosus. Lancet *384*, 1878–1888.

Marcinkiewcz, C.A., Mazzone, C.M., D'Agostino, G., Halladay, L.R., Hardaway, J.A., DiBerto, J.F., Navarro, M., Burnham, N., Cristiano, C., Dorrier, C.E., et al. (2016). Serotonin engages an anxiety and fear-promoting circuit in the extended amygdala. Nature *537*, 97–101.

Mederos, S., González-Arias, C., and Perea, G. (2018). Astrocyte–Neuron Networks: A Multilane Highway of Signaling for Homeostatic Brain Function. Front. Synaptic Neurosci. *10*.

Miao, Z., Deng, K., Wang, X., and Zhang, X. (2018). DEsingle for detecting three types of differential expression in single-cell RNA-seq data. Bioinformatics *34*, 3223–3224.

Michaelis, K.A., Norgard, M.A., Levasseur, P.R., Olson, B., Burfeind, K.G., Buenafe, A.C., Zhu, X., Jeng, S., McWeeney, S.K., and Marks, D.L. (2019). Persistent Toll-like receptor 7 stimulation induces behavioral and molecular innate immune tolerance. Brain. Behav. Immun. *82*, 338–353.

Moffitt, J.R., Bambah-Mukku, D., Eichhorn, S.W., Vaughn, E., Shekhar, K., Perez, J.D., Rubinstein, N.D., Hao, J., Regev, A., Dulac, C., et al. (2018). Molecular, spatial, and functional single-cell profiling of the hypothalamic preoptic region. Science (80-.). *362*.

Morel, L., Blenman, K.R., Croker, B.P., and Wakeland, E.K. (2001). The major murine systemic lupus erythematosus susceptibility locus, Sle1, is a cluster of functionally

related genes. Proc. Natl. Acad. Sci. U. S. A. *98*, 1787–1792.

Moulton, V.R., Suarez-Fueyo, A., Meidan, E., Li, H., Mizui, M., and Tsokos, G.C. (2017). Pathogenesis of Human Systemic Lupus Erythematosus: A Cellular Perspective. Trends Mol. Med. *23*, 615–635.

Nehar-Belaid, D., Hong, S., Marches, R., Chen, G., Bolisetty, M., Baisch, J., Walters, L., Punaro, M., Rossi, R.J., Chung, C.-H., et al. (2020). Mapping systemic lupus erythematosus heterogeneity at the single-cell level. Nat. Immunol. *21*, 1094–1106.

Oke, V., Gunnarsson, I., Dorschner, J., Eketjäll, S., Zickert, A., Niewold, T.B., and Svenungsson, E. (2019). High levels of circulating interferons type I, type II and type III associate with distinct clinical features of active systemic lupus erythematosus. Arthritis Res. Ther. *21*, 1–11.

Pablo, J.L., Wang, C., Presby, M.M., and Pitt, G.S. (2016). Polarized localization of voltage-gated Na + channels is regulated by concerted FGF13 and FGF14 action. Proc. Natl. Acad. Sci. *113*, E2665–E2674.

Palla, G., Spitzer, H., Klein, M., Fischer, D., Schaar, A.C., Kuemmerle, L.B., Rybakov, S., Ibarra, I.L., Holmberg, O., Virshup, I., et al. (2021). Squidpy: a scalable framework for spatial single cell analysis. BioRxiv 2021.02.19.431994.

Pan, W., Banks, W.A., and Kastin, A.J. (1997). Permeability of the blood-brain and blood-spinal cord barriers to interferons. J. Neuroimmunol. *76*, 105–111.

Phipson, B., Zappia, L., and Oshlack, A. (2017). Gene length and detection bias in single cell RNA sequencing protocols. F1000Research *6*, 595.

Raudvere, U., Kolberg, L., Kuzmin, I., Arak, T., Adler, P., Peterson, H., and Vilo, J. (2019). g:Profiler: a web server for functional enrichment analysis and conversions of

gene lists (2019 update). Nucleic Acids Res. *47*, W191–W198.

Reyes-Vazquez, C., Prieto-Gomez, B., and Dafny, N. (1982). Novel effects of interferon on the brain: Microiontophoretic application and single cell recording in the rat. Neurosci. Lett. *34*, 201–206.

Rodero, M.P., Decalf, J., Bondet, V., Hunt, D., Rice, G.I., Werneke, S., McGlasson, S.L., Alyanakian, M.A., Bader-Meunier, B., Barnerias, C., et al. (2017). Detection of interferon alpha protein reveals differential levels and cellular sources in disease. J. Exp. Med. *214*, 1547–1555.

Roy, E.R., Zheng, H., and Cao, W. (2020). Type I interferon response drives neuroinflammation and synapse loss in Alzheimer disease. J Clin Invest *130*, 1912–1930.

Rusinova, I., Forster, S., Yu, S., Kannan, A., Masse, M., Cumming, H., Chapman, R., and Hertzog, P.J. (2013). INTERFEROME v2.0: An updated database of annotated interferon-regulated genes. Nucleic Acids Res. *41*, 1040–1046.

Schaefer, M., Engelbrechta, M.A., Gut, O., Fiebich, B.L., Bauer, J., Schmidt, F., Grunze, H., and Lieb, K. (2002). Interferon alpha (IFNα) and psychiatric syndromes: A review. Prog. Neuro-Psychopharmacology Biol. Psychiatry *26*, 731–746.

Schreiber, G., and Piehler, J. (2015). The molecular basis for functional plasticity in type I interferon signaling. Trends Immunol. *36*, 139–149.

Schroeder, M. K., Liu, B., Hinshaw, R. G., Park, M. A., Wang, S., Dubey, S., ... & Lemere, C. A. (2021). Long-term sex-and genotype-specific effects of 56Fe irradiation on wild-type and APPswe/PS1dE9 transgenic mice. International journal of molecular sciences. *22*(24), 13305.

Schwartz, N., Stock, A.D., and Putterman, C. (2019). Neuropsychiatric lupus: new mechanistic insights and future treatment directions. Nat. Rev. Rheumatol. *15*, 137–152.

Scofield, R.H., Bruner, G.R., Namjou, B., Kimberly, R.P., Ramsey-Goldman, R., Petri, M., Reveille, J.D., Alarcón, G.S., Vilá, L.M., Reid, J., et al. (2008). Klinefelter's syndrome (47,XXY) in male systemic lupus erythematosus patients: Support for the notion of a gene-dose effect from the X chromosome. Arthritis Rheum. *58*, 2511–2517.

Seiler, S., and Tønnessen, E. (2009). Intervals , Thresholds , and Long Slow Distance□: the Role of Intensity and Duration in Endurance Training. Sportscience 32–53.

Shaw, A.E., Hughes, J., Gu, Q., Behdenna, A., Singer, J.B., Dennis, T., Orton, R.J., Varela, M., Gifford, R.J., Wilson, S.J., et al. (2017). Fundamental properties of the mammalian innate immune system revealed by multispecies comparison of type I interferon responses. PLoS Biol. *15*, 1–23.

Shiozawa, S., Kuroki, Y., Kim, M., Hirohata, S., and Ogino, T. (1992). Interferon alpha in lupus psychosis. Arthritis Rheum. *35*, 417–422.

Stuart, T., Butler, A., Hoffman, P., Hafemeister, C., Papalexi, E., Mauck, W.M., Hao, Y., Stoeckius, M., Smibert, P., and Satija, R. (2019). Comprehensive Integration of Single-Cell Data. Cell *177*, 1888-1902.e21.

Subramanian, S., Tus, K., Li, Q.Z., Wang, A., Tian, X.H., Zhou, J., Liang, C., Bartov, G., McDaniel, L.D., Zhou, X.J., et al. (2006). A Tlr7 translocation accelerates systemic autoimmunity in murine lupus. Proc. Natl. Acad. Sci. U. S. A. *103*, 9970–9975.

Südhof, T.C. (2017). Synaptic Neurexin Complexes: A Molecular Code for the Logic of Neural Circuits. Cell *171*, 745–769.

Tsokos, G.C. (2011). Systemic Lupus Erythematosus. N. Engl. J. Med. *365*, 2110–2121.

Uematsu, S., and Akira, S. (2007). Toll-like Receptors and Type I Interferons. J. Biol. Chem. *282*, 15319–15323.

Valentine, A.D., and Meyers, C.A. (2005). Neurobehavioral effects of interferon therapy. Curr. Psychiatry Rep. *7*, 391–395.

Varley, J.A., Andersson, M., Grant, E., Berretta, A., Zandi, M.S., Bondet, V., Duffy, D., Hunt, D., Piehl, F., Waters, P., et al. (2020). Absence of Neuronal Autoantibodies in Neuropsychiatric Systemic Lupus Erythematosus. Ann. Neurol. *88*, 1244–1250.

Venkatraman, A., Edlow, B.L., and Immordino-Yang, M.H. (2017). The brainstem in emotion: A review. Front. Neuroanat. *11*, 1–12.

Wang, W., Xu, L., Brandsma, J.H., Wang, Y., Hakim, M.S., Zhou, X., Yin, Y., Fuhler, G.M., Van Der Laan, L.J.W., Van Der Woude, C.J., et al. (2016). Convergent Transcription of Interferon-stimulated Genes by TNF-α and IFN-α Augments Antiviral Activity against HCV and HEV. Sci. Rep. *6*, 1–14.

Wolf, F.A., Angerer, P., and Theis, F.J. (2018). SCANPY: large-scale single-cell gene expression data analysis. Genome Biol. *19*, 15.

Yilmaz, M., Yalcin, E., Presumey, J., Aw, E., Ma, M., Whelan, C.W., Stevens, B., McCarroll, S.A., and Carroll, M.C. (2021). Overexpression of schizophrenia susceptibility factor human complement C4A promotes excessive synaptic loss and behavioral changes in mice. Nat. Neurosci. *24*, 214–224.

Zhang, L., Fu, T., Yin, R., Zhang, Q., and Shen, B. (2017). Prevalence of depression and anxiety in systemic lupus erythematosus: a systematic review and meta-analysis.

BMC Psychiatry *17*, 70.

Zhuang, H., Szeto, C., Han, S., Yang, L., and Reeves, W.H. (2015a). Animal models of interferon signature positive lupus. Front. Immunol. *6*, 6–11.

8. Data Accessibility Statement

Raw and processed sNucSeq data discussed in this publication will be deposited in NCBI's Gene Expression Omnibus (Edgar et al., 2002) and will be accessible through a GEO Series accession number. Raw and processed data for MERFISH supporting the findings of this study are located on the local Moffitt Lab server of the Boston Children's Hospital Program in Cellular and Molecular Medicine, available upon request.

9. Funding Sources

10. Figure and Table Legends

Figure 1. Temporal profiling of peripheral autoimmune correlates in the *Sle1, Yaa* mouse model. (A) Age matched B6 and *Sle1, Yaa* male mice were serially bled every 2 weeks starting from 6 weeks of age (N=10 per group). The peripheral blood ISG index was calculated using the geometric mean of $\Delta\Delta C_t$ normalized gene expression values of the following ISGs: *Mx1*, *Ifit3*, *Oas2*, *Isg15*, and *Rsad2*. 1 B6 mouse died at week 14, and 1 *Sle1, Yaa* mouse died at week 20; data points for these mice were included in statistical analyses up until the point of death. Statistics were calculated with two-way

fixed effects ANOVA, and *post hoc* comparisons were corrected using Sidak's method. **(B)** Serum IFNα was assessed across the 8 week (N=8, B6; N=9, *Sle1, Yaa*), 14 week (N=12, B6; N=15, *Sle1, Yaa*), and 20 week (N=15, B6; N=19, *Sle1, Yaa*) age groups. Statistics were calculated with two-way fixed effects ANOVA, and *post hoc* comparisons were corrected using Tukey's method. **(C)** Serum autoantibody titers targeting 19 different autoantigens were assessed across the 8 week (N=8, B6; N=9, *Sle1, Yaa*), 14 week (N=12, B6; N=15, *Sle1, Yaa*), and 20 week (N=7, B6; N=8, *Sle1, Yaa*) age groups. The autoantibody score was computed by taking the geometric mean of MFI values across 19 autoantigens per sample. Statistics were calculated with two-way fixed effects ANOVA, and *post hoc* comparisons were corrected using Sidak's method. *n.s., p>0.05; *, p<0.05; **, p<0.01; ***, p<0.001*

Supplementary Figure 1. **Cytokine and autoantibody titers across age groups in *Sle1, Yaa* mice (red) compared to B6 controls (black). (A)** Fold change expression relative to B6 controls were calculated as the $ΔΔC_t$ normalized gene expression values for the following ISGs: *Mx1*, *Ifit3*, *Oas2*, *Isg15*, and *Rsad2*. Statistics were calculated with two-way fixed effects ANOVA, and *post hoc* comparisons were corrected using Sidak's method. **(B)** Data on other serum cytokines profiled through the VeriPlex Mouse Cytokine 9-Plex ELISA Kit (PBL Assay Science), across the 8 week (N=8, B6; N=9, *Sle1, Yaa*), 14 week (N=12, B6; N=15, *Sle1, Yaa*), and 20 week (N=15, B6; N=19, *Sle1, Yaa*) age groups. Statistics were calculated with two-way fixed effects ANOVA, and *post hoc* comparisons were corrected using Sidak's method. Correlation heatmap shows Spearman rank correlations between different cytokines. **(C)** Data on individual serum autoantibodies profiled using the Luminex Human Autoimmune Autoantibody Panel

(HAIAB-10K, Millipore Sigma), across the 8 week (N=8, B6; N=9, *Sle1, Yaa*), 14 week (N=12, B6; N=15, *Sle1, Yaa*), and 20 week (N=7, B6; N=8, *Sle1, Yaa*) age groups. Statistics were calculated with two-way fixed effects ANOVA, and *post hoc* comparisons were corrected using Tukey's method. Correlation heatmap shows Spearman rank correlations between different autoantibodies. *n.s., p>0.05; *, p<0.05; **, p<0.01; ***, p<0.001*

Figure 2. **Anxiety- and fatigue-like behavioral phenotypes in the *Sle1, Yaa* mouse model. (A)** The bright open field test measures anxiety by the exploratory behavior of the subject in the brightly lit center of an open field enclosure as opposed to its periphery. *Sle1, Yaa* mice moved and spent less time in the brightly lit center field. **(B)** The light-dark box test measures anxiety by the exploratory behavior of the subject in the brightly lit half of an enclosure as opposed to the dark, covered half. *Sle1, Yaa* mice displayed less exploratory behavior in the brightly lit half of the box. **(C)** The locomotor test measures general exploratory behavior in a low stress environment. *Sle1, Yaa* mice displayed less locomotive and vertical exploratory behavior compared to B6 controls. **(D)** The rotarod test measures general motor function abilities. *Sle1, Yaa* mice showed decreased ability to stay on the accelerating rod compared to B6 controls. **(E)** The grip strength test measures general muscular strength. *Sle1, Yaa* mice displayed increased muscular weakness compared to B6 controls. **(F)** The treadmill fatigue test measures the exercise induced fatigue threshold. *Sle1, Yaa* mice showed an increased propensity to fatigue compared to B6 controls. Post-exercise lactate levels did not show any differences, suggesting that the fatigue-like phenotype is unlikely to be driven by muscular deficiencies, but possibly neuroinflammatory factors. Extrapolating from the

well-established 3-zone exercise intensity threshold for humans (Seiler and Tønnessen, 2009), and based on our own experience, the mice did not reach the limit of their aerobic capacity; exceeding this limit would have resulted in a sharp spike of blood lactate above 10mM as mice switched to anaerobic glycolysis. Sample sizes are as follows: B6 (N=18), *Sle1, Yaa* (N=17) for (A) – (E); B6 (N=11), *Sle1, Yaa* (N=12) for (F). Data were analyzed using either Student's t test or Mann-Whitney U test, assessed by normality of data distribution. *n.s., p>0.05; *, p<0.05; **, p<0.01; ***, p<0.001*

Supplementary Figure 2. **Additional behavioral tests and tissue histology support behavioral phenotypes. (A)** The elevated plus maze (EPM) test measures anxiety by the exploratory behavior of the subject in the open arm of the maze. *Sle1, Yaa* mice showed trends toward decreased exploratory behavior in the open arm. **(B)** The wire hang test measures muscular endurance by the latency to fall from an aversive, elevated height. *Sle1, Yaa* mice showed trends toward decreased holding impulse compared to B6 controls. Body weight differences were accounted for by calculating the holding impulse. **(C)** The gait test measures sensorimotor coordination by assessment of the degree of deviation from multiple body axes during the process of locomotive activity. *Sle1, Yaa* mice did not exhibit any differences in motor coordination compared to B6 controls, suggesting an unlikely contribution of ataxia to the locomotive phenotypes described. **(D)** Representative H&E images of longitudinal triceps, quadriceps, wrist, and ankle tissue sections from 20 week old B6 and *Sle1, Yaa* mice. Samples are representative images and were evaluated by a blinded pathologist with no observations of aberrant inflammatory pathology in any sample. Scale bar = 100μm. Sample sizes are as follows: B6 (N=18), *Sle1, Yaa* (N=17) for (A) – (C), B6 (N=5), *Sle1,*

Yaa (N=7) for (D). Data were analyzed using either Student's t test or Mann-Whitney U test, assessed by normality of data distribution. *n.s., p>0.05; *, p<0.05; **, p<0.01; ***, p<0.001*

Supplementary Figure 3. **Behavioral phenotypes persist through 20 weeks of age in *Sle1, Yaa* mice. (A)** The bright open field test did not show any statistically significant contributions of age to the anxiety-like phenotype. **(B)** The elevated plus maze (EPM) test showed similar contributions of age and genotype to the observed variance, although *post hoc* comparisons between B6 and *Sle1, Yaa* mice did not reach statistical significance. The interaction factor was not statistically significant, suggesting that the trends toward increased anxiety-like behavior in *Sle1, Yaa* are driven by genotype. **(C)** The light-dark box test did not show any statistically significant contributions of age to the anxiety-like phenotype. **(D)** The locomotor test showed a significant contribution of age to the variance observed in ambulatory distance, but less so in vertical counts. The interaction factor was not statistically significant, suggesting that differences between B6 and *Sle1, Yaa* mice are largely driven by genotype. **(E)** The rotarod test did not show any statistically significant contributions of age to the fatigue-like phenotype. **(F)** The grip strength test did not show any statistically significant contributions of age to the fatigue-like phenotype. **(G)** The wire hang test showed contributions of age and genotype to the observed variance, although *post hoc* comparisons between B6 and *Sle1, Yaa* mice did not reach statistical significance. The interaction factor was not statistically significant, suggesting that the trends toward increased fatigue-like behavior in *Sle1, Yaa* are driven by genotype. **(H)** The treadmill fatigue test did not show any statistically significant contributions of age to the fatigue-like phenotype. Note also that

there were no statistically significant differences observed in post-exercise lactate levels, indicating that all mice were within similar aerobic capacity thresholds. Lactate measurements were not performed for all 20-week old mice due to insufficient availability of lactate test strips. Sample sizes are as follows: B6 (N=18, 14 week; N=10, 20 week), *Sle1, Yaa* (N=17, 14 week; N=10, 20 week). Statistics were calculated with two-way fixed effects ANOVA, and *post hoc* comparisons were corrected using Tukey's method. *n.s., p>0.05; *, p<0.05; **, p<0.01; ***, p<0.001*

Supplementary Figure 4. **Maternal inflammation and genetic drift are not significant contributors to peripheral autoimmunity and behavioral phenotypes.** **(A)** Breeding scheme detailing strategy to control for maternal inflammation and genetic drift. **(B)** 14 week old B6 and *Sle1, Yaa* male mice were bled and the peripheral blood ISG signature was quantified by qPCR. The peripheral blood ISG index was calculated using the geometric mean of $\Delta\Delta C_t$ normalized gene expression values of the following ISGs: *Mx1*, *Ifit3*, *Oas2*, *Isg15*, and *Rsad2*. Data were analyzed using either Student's t test or Mann-Whitney U test, assessed by normality of data distribution. **(C)** The bright open field test showed significant contribution of breeding to the variance observed. The interaction factor was not statistically significant, suggesting that differences between B6 and *Sle1, Yaa* mice are largely driven by genotype. **(D)** The elevated plus maze (EPM) test did not show any statistically significant contributions of breeding to the anxiety-like phenotype. **(E)** The light-dark box test did not show any statistically significant contributions of breeding to the anxiety-like phenotype. **(F)** The locomotor test did not show any statistically significant contributions of breeding to the fatigue-like phenotype. **(G)** The rotarod test did not show any statistically significant contributions of

breeding to the fatigue-like phenotype. **(H)** The grip strength test showed similar contributions of breeding and genotype to the observed variance, and *post hoc* comparisons showed statistically significant differences between normal and complex breeder *Sle1, Yaa* mice. While the interaction factor was not statistically significant, the differences observed between normal and complex breeder *Sle1, Yaa* mice suggest that this phenotype is influenced by maternal inflammation or genetic drift. **(I)** The wire hang test showed that neither breeding nor genotype contributed to the observed variance. *Post hoc* comparisons did not reveal any statistically significant differences between B6 and *Sle1, Yaa* mice. **(J)** The gait test showed a statistically significant contribution of breeding to the observed variance across the 3 parameters. *Post hoc* comparisons showed that complex breeder derived *Sle1, Yaa* mice had less motor sway compared to normal breeder derived *Sle1, Yaa* mice. In all cases, the *Sle1, Yaa* mice had equivalent or less motor sway compared to their control arms, suggesting that ataxia is not a disease phenotype in the *Sle1, Yaa* model and hence does not contribute to the fatigue-like phenotype observed. Sample sizes are as follows: complex breeder B6 (N=7), complex breeder *Sle1, Yaa* (N=14) for (B), B6 (N=18, complex breeders; N=18, normal breeders), *Sle1, Yaa* (N=15, complex breeders; N=17, normal breeders) for (C) – (J Statistics were calculated with two-way fixed effects ANOVA statistics, and *post hoc* comparisons were corrected using Tukey's method. *n.s., p>0.05; *, p<0.05; **, p<0.01; ***, p<0.001*

Figure 3. **Upregulation of the type 1 interferon response across all CNS cell types.**

(A) UMAP plot for all major cell classes within the hindbrain and hippocampus, with cell types colored by cluster. **(B)** UMAP plots of the hindbrain, separated by genotype and

colored by the ISG expression index. **(C)** UMAP plots of the hippocampus, separated by genotype and colored by the ISG expression index. **(D)** Volcano plots showing differentially expressed genes in the hindbrain and hippocampus between the B6 and *Sle1, Yaa* genotypes. ISGs were defined by querying the DE gene list with the Interferome database (Rusinova et al., 2013). Dotted lines delineate Log_2 Fold Change > 1.32 and $-\text{Log}_{10}q$ > 3.

Supplementary Figure 5. **Single nuclei sequencing (sNucSeq) protocol and quality control. (A)** Graphical outline of protocol used for single nuclei sequencing. See methods ("Single nucleus sequencing (sNucSeq) and analysis) for further details. **(B)** Dot plot of marker genes for cell class clusters identified in the hindbrain. **(C)** Dot plot of marker genes for cell class clusters identified in the hippocampus. **(D)** UMAP plots by individual samples show consistent clustering in the hindbrain. **(E)** UMAP plots by individual samples show consistent clustering in the hippocampus. For (D) and (E), the number appended at the end of each sample name indicates the technical replicate.

Supplementary Figure 6. **Pathway differences in the *Sle1, Yaa* unique subcluster of astrocytes and oligodendrocytes. (A)** Volcano plots showing differentially expressed genes in hindbrain astrocytes and oligodendrocytes. **(B)** Volcano plots showing differentially expressed genes in hippocampal astrocytes and oligodendrocytes. ISGs were defined by querying the DE gene list with the Interferome database (Rusinova et al., 2013). Dotted lines delineate Log_2 Fold Change > 1.32 and $-\text{Log}_{10}q$ > 3. **(C), (D)** Dot plots showing the top 6 enriched terms in astrocytes by brain region from the Gene Ontology, KEGG, and Reactome databases, queried using differentially expressed genes as input into the gProfiler2 package (Raudvere et al.,

2019). **(E), (F)** Dot plots showing the top 6 enriched terms in oligodendrocytes by brain region from the Gene Ontology, KEGG, and Reactome databases, queried using differentially expressed genes (Log$_2$ Fold Change > 0 = "Up", Log$_2$ Fold Change < 0 = "Down") as input into the gProfiler2 package (Raudvere et al., 2019).

Supplementary Figure 7. **Interaction Pathways in subclusters of astrocytes, oligodendrocytes, and major neuronal subsets.** Cell clusters with high ISG expression were queried using the Squidpy ligand-receptor analysis package in the **(A)** hindbrain and **(B)** hippocampus. Statistically significant interactions were further analyzed by identification of interaction partner genes that were (1) differentially expressed between B6 and *Sle1, Yaa* genotypes, and (2) ISGs, as determined by querying the Interferome database (Rusinova et al., 2013). Resulting interaction pairs are listed in **Supplementary Tables 5 and 6**.

Figure 4. **Spatially enriched patches of ISGs in the brain parenchyma of *Sle1, Yaa* mice. (A)** Uniform manifold approximation and projection (UMAP) plot for all major cell classes within the brain parenchyma, with cell types colored by cluster. **(B)** Volcano plot showing differentially expressed genes between all cell classes of the B6 and *Sle1, Yaa* genotypes. Genes belonging to the ISG class of genes are highlighted. UMAP plots comparing the ISG signature in B6 and *Sle1, Yaa* mice (N=2 per group), with clear enrichment in the *Sle1, Yaa* group. Statistically significant (*q*<0.05) genes that were part of the *a priori* defined library of ISGs were identified, and the geometric mean (ISG index) of normalized count expression across these genes was computed on a per-cell basis. ISG index-high gene expression appeared to be enriched in the vascular compartment as well as in glial cells such as astrocytes, microglia, and

oligodendrocytes. **(C)** Spatial plots of the ISG index across each individual sample, showing clustered patches of ISG index-high cells in the *Sle1, Yaa* mice. **(D)** Tiled confocal images of RNAscope *in situ* hybridized *Ifit3* probe in independent 14 week old B6 and *Sle1, Yaa* samples, showing spatial patches in the *Sle1, Yaa* genotype and validating the MERFISH observations.

Supplementary Figure 8. **Quality control metrics for MERFISH. (A)** For MERFISH decoding, the same threshold for signal intensity and RNA puncta area was applied for all samples. **(B)** Over 62% of all decoded RNAs were detected without error. As RNA detection efficiency could cause technical bias, samples within less than 40% variation in total RNA counts per cell were included in the final analyses (refer to Supplementary Table 3 column on "Total RNA counts – pre filtering"). The percentage reported above the graphs refer to the percentage of RNAs decoded using the error correcting feature of MERFISH barcode design (hamming weight = 4, hamming distance = 4). **(C)** RNA counts measured by MERFISH and bulk RNA sequencing (dataset SRR7060096 from project SRP142522) were very well correlated; the Pearson correlation coefficient was > 0.77 for all samples, comparable with previously published MERFISH datasets. **(D)** RNA counts measured by MERFISH were highly reproducible from experiment to experiment; the Pearson correlation coefficient was 0.93 between the two B6 control samples, and 0.98 between the two *Sle1, Yaa* samples. Unless otherwise noted, metrics shown are from the same representative B6 and *Sle1, Yaa* samples.

Supplementary Figure 9. **Expected cell class spatial locations and differential spatial heterogeneity in ISG expression. (A)** Spatial plots of main cell classes across the brain parenchyma, color coded similarly to the UMAP in Figure 3A. Images are from

the B6_2 sample, and are representative across all MERFISH processed samples. Note that cerebellar granule cells were not shown due to their small nucleus size and highly clustered structure, which did not allow proper segmentation by the decoding algorithm. **(B)** Spatial plots of selected differentially expressed ISGs in the Sle1, Yaa_2 sample, showing spatially heterogenous expression patterns. Spatial patterns for each gene are similar in the Sle1, Yaa_1 sample, and did not show any "patch" spatial expression pattern in either of the B6 samples.

Supplementary Figure 10. Temporal dynamics of ISG patches and differential gene expression. Example tiled confocal images of RNAscope *in situ* hybridized *Ifit3* probes in 8 week and 20 week old *Sle1, Yaa* mice, showing existence and persistence of the ISG patches early and later on during the development of peripheral autoimmunity.

Supplemental Table 1. Primer Sequences and expected band sizes for genotyping reactions.

Supplemental Table 2. List of MERFISH probes in the 224-plex gene library.

Supplemental Table 3. MERFISH metadata across four samples.

Supplemental Table 4. Single nucleus sequencing post-quality control metrics of 14-week male samples.

Supplemental Table 5. Interferon-regulated genes in interaction pathways among subclusters of astrocytes, oligodendrocytes, and major neuronal subsets in the hindbrain. The first gene in each pair corresponds to the respective cell type in the left-most column, and the second gene corresponds to the respective cell type in the top-

most row. Genes that are significantly differently expressed with respect to B6 are

colored – upregulated genes are in orange and downregulated genes are in blue.

Supplemental Table 6. Interferon-regulated genes in interaction pathways among subclusters of astrocytes, oligodendrocytes, and major neuronal subsets in the hippocampus. The first gene in each pair corresponds to the respective cell type in the left-most column, and the second gene corresponds to the respective cell type in the top-most row. Genes that are significantly differently expressed with respect to B6 are colored – upregulated genes are in orange and downregulated genes are in blue.

Figure 1

A

B

C

Figure 1. Temporal profiling of peripheral autoimmune correlates in the *Sle1, Yaa* mouse model.

Figure 2

Figure 2. Anxiety- and fatigue-like behavioral phenotypes in the *Sle1, Yaa* mouse model.
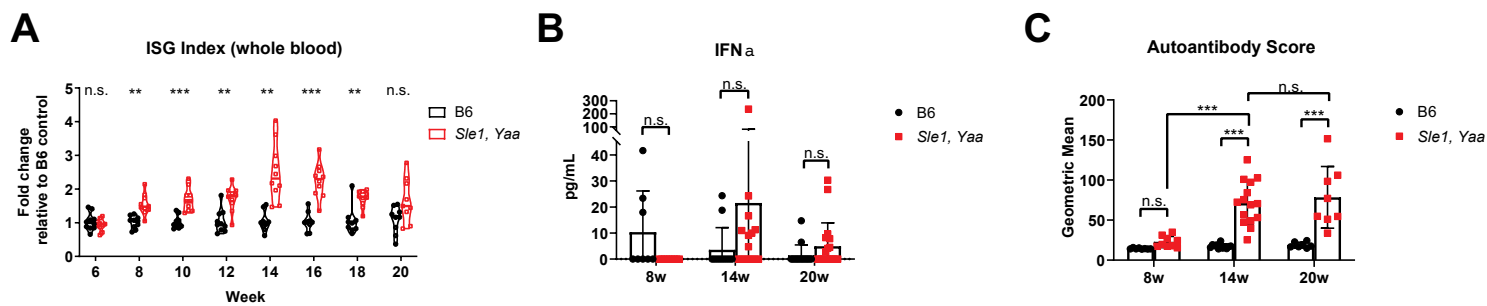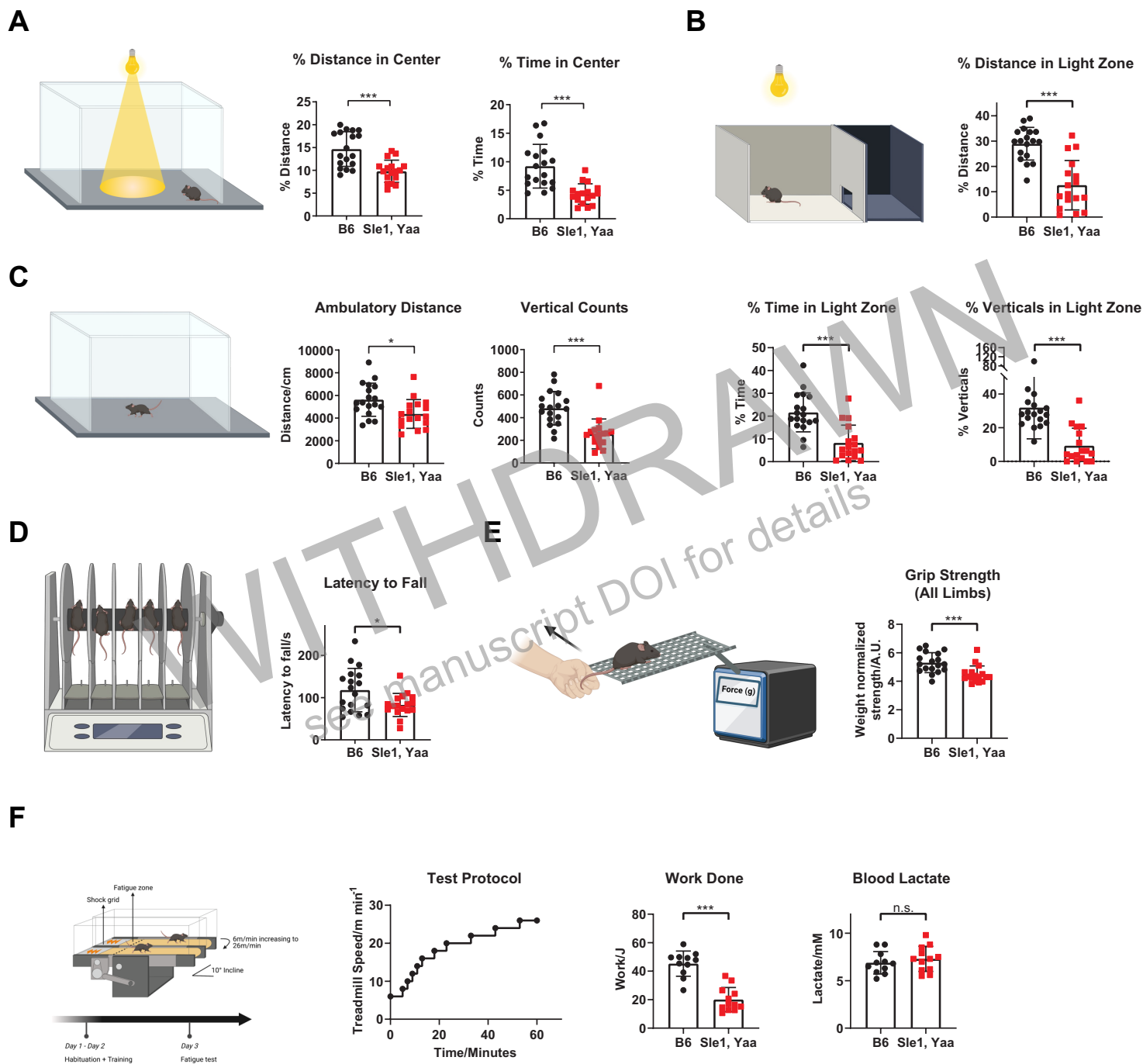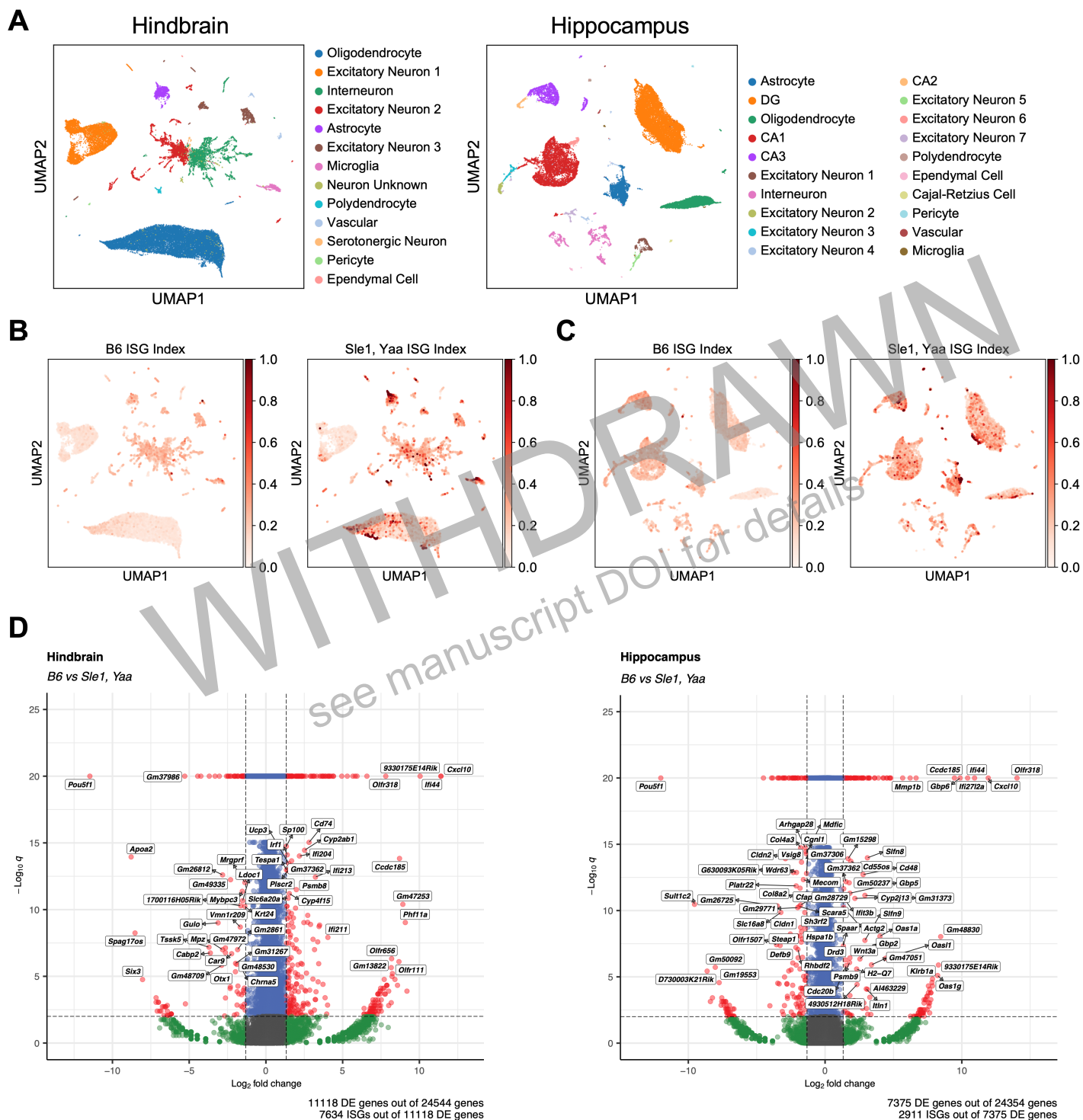
Figure 3

Figure 3. Upregulation of the type 1 interferon response across all CNS cell types.

Figure 4

Figure 4. **Spatially enriched patches of ISGs in the brain parenchyma of *Sle1, Yaa* mice.**